

Morphology and composition controlled $\text{Ga}_x\text{In}_{1-x}\text{Sb}$ nanowires: understanding ternary antimonide growth†

Cite this: *Nanoscale*, 2014, 6, 1086Sepideh Gorji Ghalamestani,^{*a} Martin Ek,^b Masoomah Ghasemi,^a Philippe Caroff,^c Jonas Johansson^a and Kimberly A. Dick^{*ab}

Antimonide-based nanowires represent an important new class of material with great promise for both fundamental physics studies and various device applications. We report a comprehensive study on understanding the growth behaviour of $\text{Ga}_x\text{In}_{1-x}\text{Sb}$ nanowires on GaAs substrates using Au nanoparticles. First, the effect of growth parameters on the morphology and composition of $\text{Ga}_x\text{In}_{1-x}\text{Sb}$ nanowires is extensively studied over the entire compositional range (from 3 to ~100% of In). Second, the obtained compositional results are explained by a kinetic model, suggesting an Arrhenius-type behavior for the trimethylindium (TMIn) precursor. Third, the particle composition is fully investigated and the implications for growth are discussed with reference to our calculated Au–Ga–In phase diagram. Fourth, a mechanism is presented to explain the temperature-dependent morphology and radial growth of the $\text{Ga}_x\text{In}_{1-x}\text{Sb}$ nanowires. Finally, we demonstrate homogeneous compositions in both axial and radial directions and the nanowires remain entirely twin-free zinc blende. The understanding gained from this study together with the potential to precisely tailor the band gap, wavelength and carrier mobilities allows fabrication of various $\text{Ga}_x\text{In}_{1-x}\text{Sb}$ -based nanowire devices.

Received 23rd September 2013
Accepted 4th November 2013

DOI: 10.1039/c3nr05079c

www.rsc.org/nanoscale

1. Introduction

The rapid progress in the development of binary III–V nanowires and their heterostructures during the last decade has demonstrated their potential as a mature nanotechnology platform for advanced energy,^{1,2} electronic,³ optoelectronic,^{4,5} and quantum devices.^{6,7} Mastering more complex materials at the nanoscale will offer richer functionalities and a steep increase in performance.^{8,9} However, the new degree of freedom offered by ternary alloying is also the source of novel material challenges. Indeed, both axial and radial compositional inhomogeneities in ternary nanowires are the rule rather than the exception,^{10–12} sometimes even leading to original self-formed segregation-induced three-dimensional (3D) patterns, especially at edges.^{8,13} The crystal structure has also been reported to be affected by alloying.^{14,15}

These difficulties arise from the interplay of several thermodynamic and kinetic effects acting in the frame of simultaneous axial nanowire growth *via* nucleation at the triple line in

Vapor–Liquid–Solid (VLS) mode under the seed particle,^{16,17} and radial growth occurring *via* a direct vapor–solid mechanism.¹⁸ Thus, the promising nanowire technology introduces new challenges that must be addressed in order to be successfully employed for various applications.

Material-wise, the antimonide family brings unique advantages complementary to other III–V nanowires, such as large wavelength coverage (from near- toward long-wavelength infrared),¹⁹ type II and type III band alignments (*e.g.* in InAs/GaSb),²⁰ useful for photodetector and solar energy applications,²¹ and the highest hole and electron mobilities, respectively for GaSb and InSb. These advantages have already been used in devices based on binary nanowires.²² Further developments will require the use of ternary Sb-based nanowires, such as $\text{GaAs}_x\text{Sb}_{1-x}$, $\text{Ga}_x\text{In}_{1-x}\text{Sb}$ and $\text{GaP}_x\text{Sb}_{1-x}$. In particular, it has been shown that the Er-doped $\text{Ga}_x\text{In}_{1-x}\text{Sb}$ alloy is a promising candidate for thermoelectricity²³ and also the nanowire geometry reduces the thermal conductivity.²⁴ Therefore, the epitaxial growth of the Er-doped $\text{Ga}_x\text{In}_{1-x}\text{Sb}$ nanowires could make a very good thermoelectric candidate in the future. However, the progress and the development of the ternary antimonide nanowires have been slow due to the rather complex growth behavior of these materials. Previously, we have demonstrated the successful growth of $\text{Ga}_x\text{In}_{1-x}\text{Sb}$ nanowires on InAs substrates by MOVPE and shown the potential to tune composition and morphology.²⁵

Here, we report on the complete growth study of the $\text{Ga}_x\text{In}_{1-x}\text{Sb}$ nanowires on GaAs substrates by Metal Organic

^aSolid State Physics, Lund University, Box 118, SE-22100 Lund, Sweden. E-mail: sepideh.gorji@ftf.lth.se

^bCenter for Analysis and Synthesis, Lund University, Box 124, SE-22100 Lund, Sweden. E-mail: kimberly.dick@ftf.lth.se

^cDepartment of Electronic Materials Engineering, Research School of Physics and Engineering, The Australian National University, Canberra, ACT 0200, Australia

† Electronic supplementary information (ESI) available. See DOI: 10.1039/c3nr05079c

Vapour Phase Epitaxy (MOVPE) and demonstrate their full-range tunability, perfect crystal structure and good compositional homogeneity. The main focus of this study is to understand the growth behavior of the $\text{Ga}_x\text{In}_{1-x}\text{Sb}$ nanowires and also the properties of their seed particles. The composition of these nanowires and their seed particles has been fully mapped out under various precursor molar fractions and temperatures using *ex situ* XEDS measurements. As a result, by tailoring the growth parameters, the composition of the grown $\text{Ga}_x\text{In}_{1-x}\text{Sb}$ nanowires is precisely controlled, covering the entire range, while maintaining a pure cubic zinc blende crystal phase. We then suggest a kinetic model to explain the composition of the grown nanowires as a function of temperature and further discuss the particle composition evolution through our calculated Au–Ga–In phase diagram. Finally, the morphology evolution of the nanowires with growth temperature has been studied and tentatively explained by a growth mechanism governing the temperature-dependent radial growth behavior of the grown $\text{Ga}_x\text{In}_{1-x}\text{Sb}$ nanowires.

2. Experimental details

The growth is performed on GaAs (111)B substrates. Au aerosol nanoparticles with various diameters in the range of 30–70 nm and the density of $1\ \mu\text{m}^{-2}$ are used to seed the nanowire growth. The growth is performed in a standard low pressure (100 mbar) horizontal MOVPE reactor (Aixtron 200/4). Trimethylindium (TMIn), trimethylgallium (TMGa), trimethylantimony (TMSb), and arsine (AsH_3) are used as the precursors. The total flow is $13\ \text{L min}^{-1}$ with hydrogen as a carrier gas. Directly after loading the samples into the reactor, the GaAs substrates are annealed at $630\ ^\circ\text{C}$. First, a short segment of GaAs is grown for 2 min with respective TMGa and AsH_3 molar fractions of 2.13×10^{-5} and 1.23×10^{-3} . Second, another short segment of GaSb is grown for 10 min following a simultaneous switch between AsH_3 and TMSb (molar fraction 6.8×10^{-5}). In the case of temperature change, after the GaAs segment growth (before the GaSb segment), the nanowires are kept only under AsH_3 flow for ~ 2 min to get to the desired growth temperature (470 – $550\ ^\circ\text{C}$). Then, the simultaneous switch between AsH_3 and TMSb is done. Finally, the top $\text{Ga}_x\text{In}_{1-x}\text{Sb}$ is grown by adding the second group III precursor (TMIn). This is performed by introducing a 30 s pause to vary TMGa to the desired value. The $\text{Ga}_x\text{In}_{1-x}\text{Sb}$ segments are grown with respective TMGa, TMIn, and TMSb molar fractions varied in the ranges of 2.13×10^{-5} to 9.1×10^{-5} , 3.87×10^{-7} to 7.52×10^{-7} , and 2.28×10^{-5} to 6.8×10^{-5} . The $\text{Ga}_x\text{In}_{1-x}\text{Sb}$ growth time is varied from 20 to 80 min. The samples are grown at various temperatures in the range of 450 – $550\ ^\circ\text{C}$. However, the GaAs stem is always grown at $450\ ^\circ\text{C}$ to ensure proper nucleation.

The grown nanowires were characterized by scanning electron microscopy (SEM) (Zeiss LEO 1560), transmission electron microscopy (TEM), and high angle annular dark field (HAADF) imaging using a scanning TEM (STEM) (JEOL 3000F). Prior to the TEM characterization, the nanowires were broken off from the substrate and mechanically transferred onto carbon Cu grids. Energy dispersive X-ray spectroscopy (XEDS) was used to

determine the composition of the nanowires and Au nanoparticles. Post-growth XEDS analysis of the Au nanoparticles may not reveal the exact *in situ* condition. However, it could provide valuable insight about the samples grown under different conditions including some trends in the Ga/In content of the particles.

3. Results and discussion

Fig. 1a shows a schematic structure of the GaAs/GaSb/ $\text{Ga}_x\text{In}_{1-x}\text{Sb}$ nanowires grown on GaAs (111)B substrates. Unlike the previously-reported InAs/InSb/ $\text{Ga}_x\text{In}_{1-x}\text{Sb}$ nanowires,²⁵ the GaAs/GaSb/ $\text{Ga}_x\text{In}_{1-x}\text{Sb}$ do not show any diameter change from the binary to the ternary antimonide segment, except at very high TMIn molar fractions (higher than $\sim 1 \times 10^{-6}$) where an almost pure InSb segment is formed. Fig. 1b shows a typical SEM image of GaAs/GaSb/ $\text{Ga}_x\text{In}_{1-x}\text{Sb}$ nanowires grown on the GaAs substrates where the bottom thinner parts correspond to the GaAs stems and the top thicker parts correspond to the GaSb and $\text{Ga}_x\text{In}_{1-x}\text{Sb}$ segments. The compositions of the grown $\text{Ga}_x\text{In}_{1-x}\text{Sb}$ nanowires were tuned by keeping the TMSb molar fraction constant and varying both TMGa and TMIn molar fractions.²⁵ Fig. 2a shows the Ga/In ratio in the solid phase (calculated from XEDS analysis) with respect to the Ga/In ratio in the vapor phase (determined by TMGa and TMIn precursor molar fractions). The blue curve in Fig. 2a shows the composition data for the samples grown at $450\ ^\circ\text{C}$ where the error bars represent standard deviation from the average values. These composition data are quite consistent with the similarly grown InAs/InSb/ $\text{Ga}_x\text{In}_{1-x}\text{Sb}$ nanowires (with the same TMSb molar fraction during $\text{Ga}_x\text{In}_{1-x}\text{Sb}$ growth).²⁵ The data show that even at the maximum possible vapor-phase Ga/In ratio achievable in our system (235), the composition of the grown nanowires is $\text{Ga}_{0.65}\text{In}_{0.35}\text{Sb}$. Therefore to further tune the composition, we studied the temperature effect on the GaAs/GaSb/ $\text{Ga}_x\text{In}_{1-x}\text{Sb}$ nanowires. It should be noted that it was not possible to perform similar temperature studies on the InAs/InSb/ $\text{Ga}_x\text{In}_{1-x}\text{Sb}$ nanowires, as the InAs stem decomposes at high temperatures.²⁶

3.1. Temperature effect

In order to study the effect of temperature on the growth of the $\text{Ga}_x\text{In}_{1-x}\text{Sb}$ nanowires, the temperature was varied after the GaAs stem growth and before the GaSb segment growth. This ensures proper GaAs nucleation and a stable temperature during the $\text{Ga}_x\text{In}_{1-x}\text{Sb}$ nanowire growth, as schematically shown in Fig. 1c.

3.1.1. Nanowire composition. The black curve in Fig. 2a shows the composition data for the nanowires grown at $470\ ^\circ\text{C}$, clearly demonstrating higher Ga/In ratio nanowires where the composition at the maximum Ga/In vapor phase is $\text{Ga}_{0.85}\text{In}_{0.15}\text{Sb}$. It should be mentioned that due to the reactor condition shift over time, this set of samples was grown with a lower Sb molar fraction of 2.28×10^{-5} , compared to the blue set grown at $450\ ^\circ\text{C}$ (Sb molar fraction of 6.84×10^{-5}). However, XEDS compositional characterization data show that this Sb molar fraction re-calibration results in the same nanowire

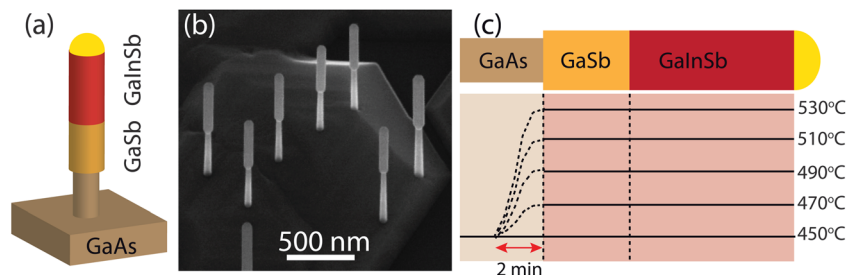


Fig. 1 (a) Schematic illustration of the GaAs/GaSb/Ga_xIn_{1-x}Sb nanowires grown on the GaAs substrate. (b) 30° tilted SEM image of the grown nanowires at 510 °C with a Ga/In vapor phase ratio of 91. (c) Schematic illustration of the temperature increase after the GaAs stem and before GaSb segment growth. The temperature was increased for 2 min (or more than 2 min) until the temperature was stabilized.

composition, compared to the previously grown nanowires with higher Sb molar fraction.

To fully understand the growth behavior of the Ga_xIn_{1-x}Sb nanowires, the temperature effect was further studied in the range of 430–550 °C. In order to perform the temperature study, three specific growth conditions were selected including high, medium, and low Ga/In vapor ratios of 235, 91, and 28, respectively.

Morphological characterization of the grown nanowires with various temperatures of 430–550 °C revealed no successful vertical nanowire growth at 430 °C. Other than that all the other growth temperatures showed successful nanowire growth. In the case of 550 °C and the highest Ga/In vapor ratio of 235, the diameter dramatically increased after the GaAs stem growth about an order of magnitude and the nanowires were terminated by huge Ga-droplets (shown in Fig. S1 of the ESI†). The compositions of the Ga_xIn_{1-x}Sb nanowires grown at temperatures from 450 to 550 °C were then studied. The red, green, and black data points in Fig. 2b show the In content (measured by XEDS) with respect to the growth temperature for Ga/In vapor phase ratios of 235, 91, and 28, respectively. These data show that the In content decreases with increasing temperature and hence very low In-content Ga_xIn_{1-x}Sb nanowires (below 5% In) could be grown at high temperatures (510 °C and higher).

Further compositional studies on the grown nanowires indicate the growth of Ga_xIn_{1-x}Sb shells around the GaSb/Ga_xIn_{1-x}Sb core nanowires. It should be noted that the shell thickness decreases for the samples grown at higher temperatures, which is discussed further in Section 3.2. Fig. 2d and e show the HAADF STEM and XEDS compositional map of a typical grown nanowire, respectively. As shown in Fig. 2d and e, the core and shell compositions are uniform within the limits of this measurement.

3.1.2. Kinetic model. As discussed in Section 3.1.1, increasing the growth temperature results in lower In-content (higher Ga-content) nanowires, consistent with a previous report for two-dimensional (2D) growth.²⁷ The reason for this type of behavior is attributed to the temperature dependent TMin and TMGa pyrolysis.

To explain this compositional trend, we propose a kinetic model which considers two parallel pathways for the TMin and TMGa precursors. According to our model (explained in more detail in the modeling part of the ESI†), the In composition in the nanowire (X_s^{In}) can be calculated from:

$$X_s^{\text{In}} = \frac{[\text{In}]^P}{[\text{In}]^P + k' \exp(-E/RT)[\text{Ga}]^P} \quad (1)$$

where rewriting eqn (1) to obtain the Arrhenius parameters including activation energy (E) and pre-exponential factor (k') results in:

$$\frac{[\text{In}]^P}{X_s^{\text{In}} - [\text{In}]^P} = k' \exp(-E/RT) \quad (2)$$

Fig. 2c shows the left hand side of the eqn (2) for the sample series with a Ga/In vapor phase ratio of 235 (red data series of Fig. 2b) with respect to the inverse of their corresponding growth temperatures. The data clearly suggest an activated growth process which saturates at higher temperatures (above 510 °C). The red line in Fig. 3c shows the exponential fit to the lower temperature range (450–510 °C), indicating an activation energy of $E = 52 \text{ kcal mol}^{-1}$ and pre-exponential factor of $k' = 4 \times 10^{13}$. This obtained activation energy value is slightly higher than the value reported by McCauley *et al.*,²⁸ suggesting that the decomposition pathway is affected by the presence of other precursors.

3.1.3. Particle composition. In addition to the nanowire composition, we have also investigated the Au nanoparticle compositions for all the grown samples. Post-growth XEDS analysis of the Au nanoparticles is not expected to reveal the exact *in situ* condition. However, comparing samples grown under different conditions may give us important clues to trends in the Ga/In content of the particles.

For all the grown samples, the particle composition is found to be an alloy of Au, In, Ga and Sb where their amounts vary depending on the corresponding growth condition. The presence of Ga in the Au nanoparticles is a surprising finding; for example in Ga_xIn_{1-x}As nanowires grown with hydride-based group V precursors, there is little or no post-growth detectable Ga in the particle since it gets emptied out during cooling (even under H₂).²⁹ Therefore, the presence of Ga could be attributed to the presence of Sb which probably changes the solubility of the group III precursors inside the nanoparticle. Post-growth nanoparticle compositional analyses on the temperature series (Section 3.1.1) also show higher Ga/In ratio for samples grown at higher temperatures. The black data points in Fig. 3a demonstrate

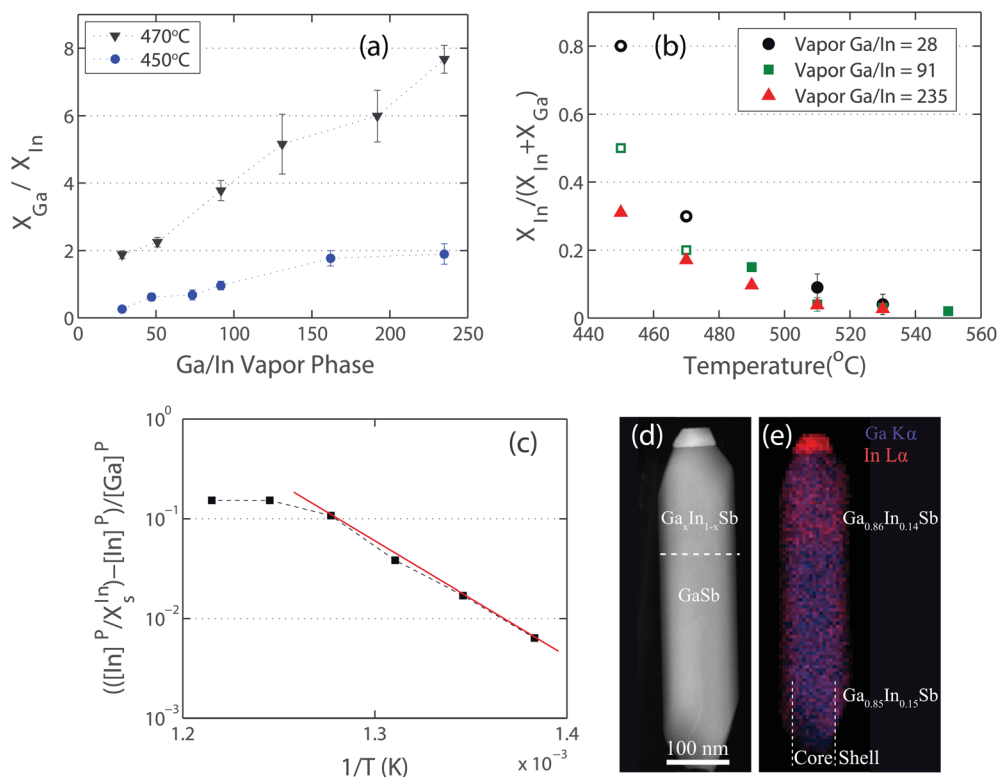


Fig. 2 (a) Ga/In ratio of the grown $\text{Ga}_x\text{In}_{1-x}\text{Sb}$ nanowires (measured by XEDS) versus the Ga/In ratio in the vapor phase (based on TMGa and TMIn precursor molar fractions). The blue and black data points correspond to the samples grown at 450 and 470 °C temperatures, respectively. (b) In-content (measured by XEDS) for three specific growth conditions of high (235), medium (91) and low (28) Ga/In vapor phase ratios (shown by respective red, green and black data points) grown at various temperatures of 450–550 °C. The open data points were grown at a different time (several months before), compared to the filled data points. The error bars in (a) and (b) represent standard deviation from the average values. (c) Arrhenius plot for the sample series grown with the highest Ga/In vapor phase ratio (235) at various temperatures of 450–530 °C. The fitted red line indicates an activation energy of 52 kcal mol⁻¹ and pre-exponential factor of 4×10^{13} . (d) HAADF STEM image and (e) overlaid Ga and In XEDS maps from a nanowire grown at 490 °C with a medium Ga/In vapor phase ratio of 91, where the $\text{Ga}_x\text{In}_{1-x}\text{Sb}$ was grown for 45 min. The XEDS quantification indicates $x = 0.86$ and $x = 0.85$ (Ga-content) for the core and the shell, respectively. This difference is within the accuracy of the XEDS method.

Ga/In ratios for the nanowires grown at various temperatures (with the highest Ga/In in the vapor phase of 235) and the blue data series shows the corresponding Ga/In ratio inside the nanoparticles. As the data suggest, the particle composition shows a similar trend to the nanowire composition. Moreover, Fig. 3b shows the group III/Au ratios for nanowires grown at various temperatures where the green and red data series correspond to the In/Au and Ga/Au ratio, respectively. As Fig. 3b suggests, there is an abrupt compositional change at 490 °C which is clarified later in the text. Similarly, the data suggest lower In (higher Ga) content for samples grown at higher temperature, consistent with the wire composition. As is known that Au has higher affinity for In than Ga,^{29,30} the results of the temperature study indicate that this parameter plays a crucial role. Furthermore, the Sb/Au ratios for samples grown at various temperatures were determined, and shown in Fig. S3 of the ESI.† It should be noted that the Sb concentration is quite low (below ~3 atomic%) and hence their standard deviations (shown by the error bars) are quite significant. However, the data suggest that the Sb content decreases for samples grown at higher temperatures. It should be noted that similar compositional

characterizations were conducted on the nanowires with medium Ga/In vapor phase ratios (91) and the results indicate similar behavior (not shown here).

To understand the particle compositional change for samples grown at various temperatures of 450–530 °C, we have calculated the phase diagram of the Au–Ga–In ternary system (based on the CALPHAD method and using Thermo-Calc software) for this temperature range (450–530 °C).³¹ We should note that to simplify the calculations we have disregarded the Sb element which might shift the corresponding phase behavior. However, we believe that the Au–Ga–In ternary system could provide us valuable information about the particle compositional trend which governs the nanowire growth. Further details of the phase diagram calculations are beyond the scope of this study and will be reported elsewhere.

Fig. 3c shows several overlaid calculated liquidus projections of the Au–Ga–In ternary system with 20 °C change for the temperature range of 450–530 °C. The particle compositions for the same set of samples, grown with the highest Ga/In ratio of 235 (Fig. 3b), are also shown in Fig. 3c. The black square, blue star, green circle, purple diamond and red triangle data points

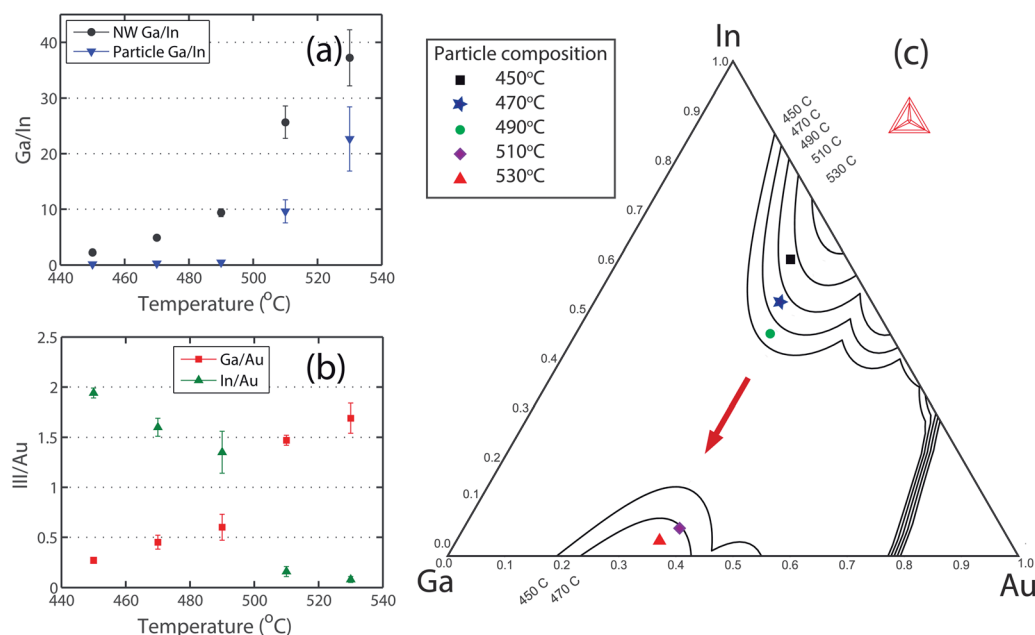


Fig. 3 (a) Ga/In ratio (calculated from XEDS measurements) for nanowires and particles grown at various temperatures of 450–530 °C (with the highest Ga/In in the vapor phase of 235) is shown by black and blue data points, respectively. The data suggest similar trends for the nanowire and the corresponding particle composition, indicating a higher Ga/In ratio for samples grown at higher temperatures. (b) In/Au (green data points) and Ga/Au ratio (red data points) for samples grown at various temperatures of 450–530 °C, suggesting lower In (higher Ga) for higher temperatures. (c) Several overlaid calculated liquidus projections for the temperature range of 450–530 °C together with particle compositions for the samples grown with a high Ga/In ratio of 235, indicating an abrupt particle compositional change for high temperatures (above 490 °C), shown by a red arrow.

correspond to the temperatures of 450, 470, 490, 510 and 530 °C, respectively. As shown in Fig. 3c, above 490 °C growth temperature (green data point), there is a large compositional change in the samples grown at higher temperatures (purple and red data points), shown by a red arrow. The high temperature grown samples (above 490 °C) are quite close to the Ga-rich corner. This abrupt compositional change might originate from several factors such as drastic change of the diffusion length, effective V/III ratio (related to the enhanced pyrolysis at higher temperatures), and also from a particle phase change from solid to liquid so that the growth for temperatures higher than 490 °C occurs *via* a liquid particle (solid for the rest). In fact, the VLS growth mechanism is the most widely known nanowire growth mechanism.³² On the other hand, the Vapor-Solid-Solid (VSS) growth mode has also been observed in several material systems.^{33,34} It should be mentioned that similar argument could be used to explain particle compositional change for samples grown with the medium Ga/In vapor phase ratio (91).

3.2. Nanowire morphology

Apart from the composition, temperature also affects the morphology of the $\text{Ga}_x\text{In}_{1-x}\text{Sb}$ nanowires. The results indicate that nanowires grown at lower temperatures have substantial radial growth, compared to those grown at higher temperatures. Fig. 4a–e show SEM images of the set of nanowires grown at various temperatures of 450–530 °C, clearly demonstrating less radial and more axial growth for the higher temperature grown nanowires.

The filled black circle and blue square data points in Fig. 4f show the measured length and diameter (for both GaSb and $\text{Ga}_x\text{In}_{1-x}\text{Sb}$) for the samples shown in Fig. 4a–e. As there is no diameter change from the GaSb to the $\text{Ga}_x\text{In}_{1-x}\text{Sb}$ segments, a separate set of GaAs/GaSb nanowires was grown at various temperatures to compare the axial and radial growth rates. The open black circle and blue square data points show the respective length and diameter of the GaSb reference samples. As the data suggest, the increase in the nanowire length is related to the increase in the axial growth rate of the GaSb segments at higher temperatures.³⁵ However, the significant radial growth at lower temperatures is related to the $\text{Ga}_x\text{In}_{1-x}\text{Sb}$ segment. In other words, the total volume is not constant. It should also be noted that the radial growth rate is highest in the temperature series for samples with the lowest Ga content (lowest temperature), while our previous study showed the highest radial growth rate for nanowires with highest Ga content (high Ga/In ratio in the vapor).²⁵ This suggests that the radial growth rate is not directly connected to the $\text{Ga}_x\text{In}_{1-x}\text{Sb}$ composition.

We attribute this reduction of radial growth (at higher temperatures) to the low InSb decomposition temperature.³⁶ As shown in Fig. 4g, the nanowire radial growth occurs *via* transport of either completely or partially decomposed precursors to the nanowire side facets. In the case of In adatoms, they either bind to existing Sb sites or to incoming Sb precursors (physisorbed state). In the high temperature regime, mainly temperatures above 490 °C (Fig. 4d and e), these InSb bonds do not chemisorb and leave from the nanowire side facets.

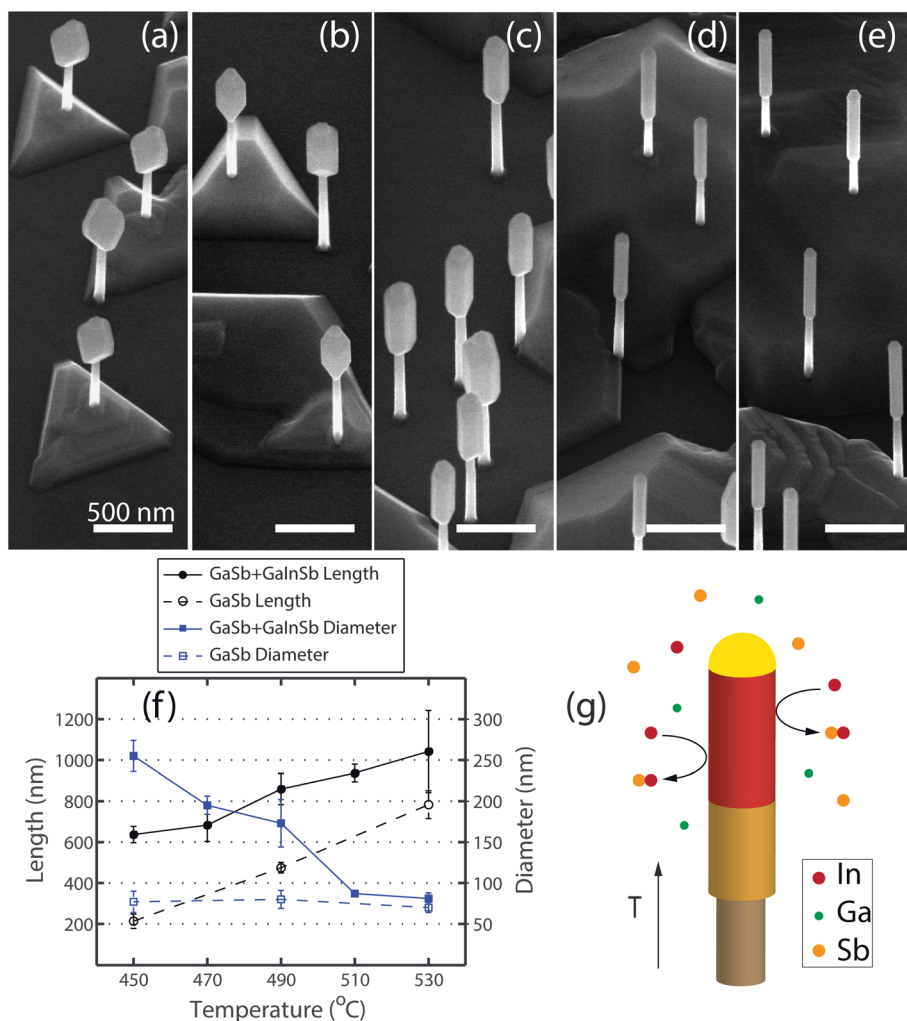


Fig. 4 30° tilted SEM images of GaAs/GaSb/Ga_xIn_{1-x}Sb nanowires grown at various temperatures of (a) 450 °C (b) 470 °C (c) 490 °C (d) 510 °C (e) 530 °C, demonstrating significant radial growth for lower temperatures. All the nanowires are seeded with 50 nm diameter Au nanoparticles and grown with the medium Ga/In vapor ratio of 91. (f) Corresponding length and diameter of the nanowires (shown in (a)–(e)), demonstrating less radial and more axial growth for the nanowires grown at higher temperatures. (g) Schematic illustration of InSb evaporation from the InSb side facets at high temperatures, resulting in the suppression of radial growth.

Therefore, the removal of Sb (together with In) does not allow further Ga binding and suppresses the radial growth. Pea *et al.* have shown a similar temperature effect on the InAsSb nanowires and related the suppression of the radial growth to the larger evaporation from the nanowire side facets.³⁷ Furthermore, it should be noted that as the growth temperature increases the volume of the parasitic substrate surface growth increases, as high growth temperatures favor 2D growth (see Fig. 4a–e).

Finally, we have investigated the growth rate of the Ga_xIn_{1-x}Sb nanowires by growing a series of samples with varied total growth time. Fig. S4 of the ESI† shows the growth rate of the nanowires grown at 510 °C with a medium Ga/In vapor phase ratio (91). The results show a very low growth rate (~3 nm min⁻¹), consistent with the previous report on the InAs substrate.²⁵ There is also a weak trend that higher TMIn and TMGa molar fractions increase the axial and radial growth rates respectively, consistent with the previous report.²⁵

4. Conclusion

In summary, we have grown Ga_xIn_{1-x}Sb nanowires on GaAs substrates and investigated the effect of the growth parameters on the nanowires composition and morphology. The compositional analysis indicates that increasing the Ga/In ratio and in particular temperature results in higher Ga-content Ga_xIn_{1-x}Sb nanowires. By tuning the growth parameters, the composition of the grown Ga_xIn_{1-x}Sb nanowires is precisely controlled over the entire range, while maintaining a pure zinc blende crystal phase and good compositional homogeneity. Furthermore, the temperature effect on the nanowire composition is explained by our proposed kinetic model, indicating an Arrhenius-type behavior. In addition, the composition of the catalyst particles is measured by XEDS analysis and compared with our calculated Au–Ga–In phase diagram. Finally, the morphological characterization of the grown nanowires shows that higher temperatures result in less radial growth, which can be

explained by increased evaporation from the nanowire side facets. These grown $\text{Ga}_x\text{In}_{1-x}\text{Sb}$ nanowires with precisely controlled composition and morphology are promising building blocks for several applications such as high speed n- and p-type nanoelectronic devices.

Acknowledgements

This work was supported by the Swedish Research Council (VR), the Swedish Foundation for Strategic Research (SSF), VINNOVA, the Knut and Alice Wallenberg Foundation (KAW), and by the Nanometer Structure Consortium at Lund University (nmC@LU). P.C. is the recipient of an Australian Research Council Future Fellowship (project number FT120100498).

Notes and references

- 1 J. Wallentin, N. Anttu, D. Asoli, M. Huffman, I. Åberg, M. H. Magnusson, G. Siefer, P. Fuss-Kailuweit, F. Dimroth, B. Witzigmann, H. Q. Xu, L. Samuelson, K. Deppert and M. T. Borgström, *Science*, 2013, **339**, 1057.
- 2 P. Krogstrup, H. I. Jørgensen, M. Heiss, O. Demichel, J. V. Holm, M. Aagesen, J. Nygard and A. Fontcuberta i Morral, *Nat. Photonics*, 2013, **7**, 306.
- 3 A. W. Dey, J. Svensson, B. M. Borg, M. Ek and L.-E. Wernersson, *Nano Lett.*, 2012, **12**, 5593.
- 4 J. C. Johnson, H.-J. Choi, K. P. Knutsen, R. D. Schaller, P. Yang and R. J. Saykally, *Nat. Mater.*, 2002, **1**, 106.
- 5 B. Piccione, C.-H. Cho, L. K. van Vugt and R. Agarwal, *Nat. Nanotechnol.*, 2012, **7**, 640–645.
- 6 S. Nadj-Perge, S. M. Frolov, E. P. A. M. Bakkers and L. P. Kouwenhoven, *Nature*, 2010, **468**, 1084.
- 7 V. Mourik, K. Zuo, S. M. Frolov, S. R. Plissard, E. P. A. M. Bakkers and L. P. Kouwenhoven, *Science*, 2012, **336**, 1003.
- 8 M. Heiss, Y. Fontana, A. Gustafsson, G. Wüst, C. Magen, D. D. O'Regan, J. W. Luo, B. Ketterer, S. Conesa-Boj, A. V. Kuhlmann, J. Houel, E. Russo-Averchi, J. R. Morante, M. Cantoni, N. Marzari, J. Arbiol, A. Zunger, R. J. Warburton and A. Fontcuberta i Morral, *Nat. Mater.*, 2013, **12**, 439.
- 9 K. Tomioka, M. Yoshimura and T. Fukui, *Nature*, 2012, **488**, 189.
- 10 P. K. Mohseni, A. Behnam, J. D. Wood, C. D. English, J. W. Lyding, E. Pop and X. Li, *Nano Lett.*, 2013, **13**, 1153.
- 11 Y.-N. Guo, H.-Y. Xu, G. J. Auchterlonie, T. Burgess, H. J. Joyce, Q. Gao, H. H. Tan, C. Jagadish, H.-B. Shu, X.-S. Chen, W. Lu, Y. Kim and J. Zou, *Nano Lett.*, 2013, **13**, 643.
- 12 Y. Zhang, M. Aagesen, J. V. Holm, H. I. Jørgensen, J. Wu and H. Liu, *Nano Lett.*, 2013, **13**, 3897.
- 13 N. Sköld, J. B. Wagner, G. Karlsson, T. Hernan, W. Seifert, M.-E. Pistol and L. Samuelson, *Nano Lett.*, 2006, **6**, 2743.
- 14 C. S. Jung, H. S. Kim, G. B. Jung, K. J. Gong, Y. J. Cho, S. Y. Jang, C. H. Kim, C.-W. Lee and J. Park, *J. Phys. Chem. C*, 2011, **115**, 7843.
- 15 T. Xu, K. A. Dick, S. Plissard, T. H. Nguyen, Y. Makoudi, M. Berthe, J.-P. Nys, X. Wallart, B. Grandidier and P. Caroff, *Nanotechnology*, 2012, **23**, 095702.
- 16 F. Glas, J.-C. Harmand and G. Patriarche, *Phys. Rev. Lett.*, 2007, **99**, 146101.
- 17 B. A. Wacaser, K. A. Dick, J. Johansson, M. T. Borgström, K. Deppert and L. Samuelson, *Adv. Mater.*, 2009, **21**, 153.
- 18 M. C. Plante and R. R. LaPierre, *J. Appl. Phys.*, 2009, **105**, 114304.
- 19 J. Svensson, N. Anttu, N. Vainorius, B. M. Borg and L.-E. Wernersson, *Nano Lett.*, 2013, **13**, 1380.
- 20 B. M. Borg, K. A. Dick, B. Ganjipour, M.-E. Pistol, L.-E. Wernersson and C. Thelander, *Nano Lett.*, 2010, **10**, 4080.
- 21 S. S. Lo, T. Mirkovic, C.-H. Chuang, C. Burda and G. D. Scholes, *Adv. Mater.*, 2011, **23**, 180.
- 22 A. W. Dey, B. M. Borg, B. Ganjipour, M. Ek, K. A. Dick, E. Lind, C. Thelander and L.-E. Wernersson, *IEEE Electron Device Lett.*, 2013, **34**, 211.
- 23 J. P. Feser, D. Xu, H. Lu, Y. Zhao, A. Shakouri, A. C. Gossard and A. Majumdar, *Appl. Phys. Lett.*, 2013, **103**, 103102.
- 24 F. Zhou, A. L. Moore, J. Bolinsson, A. Persson, L. Fröberg, M. T. Pettes, H. Kong, L. Rabenberg, P. Caroff, D. A. Stewart, N. Mingo, K. A. Dick, L. Samuelson, H. Linke and L. Shi, *Phys. Rev. B: Condens. Matter Mater. Phys.*, 2011, **83**, 205416.
- 25 S. Gorji Ghalamestani, M. Ek, B. Ganjipour, C. Thelander, J. Johansson, P. Caroff and K. A. Dick, *Nano Lett.*, 2012, **12**, 4914.
- 26 S. Gorji Ghalamestani, M. Heurlin, L.-E. Wernersson, S. Lehmann and K. A. Dick, *Nanotechnology*, 2012, **23**, 285601.
- 27 A. Aardvark, N. J. Mason and P. J. Walker, *Prog. Cryst. Growth Charact.*, 1997, **35**, 207.
- 28 J. A. McCaulley, R. J. Shul and V. M. Donnelly, *J. Vac. Sci. Technol.*, A, 1991, **9**, 2872.
- 29 K. A. Dick, J. Bolinsson, B. M. Borg and J. Johansson, *Nano Lett.*, 2012, **12**, 3200.
- 30 M. Paladugu, J. Zou, Y.-N. Guo, X. Zhang, Y. Kim, H. J. Joyce, Q. Gao, H. H. Tan and C. Jagadish, *Appl. Phys. Lett.*, 2008, **93**, 101911.
- 31 J.-O. Andersson, T. Helander, L. Höglund, P. Shi and B. Sundman, *Calphad*, 2002, **26**, 273.
- 32 R. S. Wagner and W. C. Ellis, *Appl. Phys. Lett.*, 1964, **4**, 89.
- 33 A. I. Persson, M. W. Larsson, S. Stenström, B. J. Ohlsson, L. Samuelson and L. R. Wallenberg, *Nat. Mater.*, 2004, **3**, 677.
- 34 S. Kodambaka, J. Tersoff, M. C. Reuter and F. M. Ross, *Science*, 2007, **316**, 729.
- 35 K. A. Dick, K. Deppert, L. S. Karlsson, L. R. Wallenberg, L. Samuelson and W. Seifert, *Adv. Funct. Mater.*, 2005, **15**, 1603.
- 36 M. Yano, H. Yokose, Y. Iwai and M. Inoue, *J. Cryst. Growth*, 1991, **111**, 609.
- 37 M. Pea, D. Ercolani, A. Li, M. Gemmi, F. Rossi, F. Beltram and L. Sorba, *J. Cryst. Growth*, 2013, **366**, 8.